# *RLC* Parameters Measurement and Fusion for High-Sensitivity Inductive Sensors

Dong Liu, Hong Zhang, Xiaoting Xiao, Qiuping Ma, Haoran Li, Guiyun Tian, *Senior Member, IEEE*, Bin Gao, *Senior Member, IEEE*, and Jianbo Wu

***Abstract*— In this article, an equivalent conversion between eddy current (ECT) sensor topology circuit and piezoelectric crystal topology circuit is proposed. Based on this conversion, a novel multiparameters separation method is designed to identify the inductance, capacitance, and resistance of the ECT sensor topology circuit though frequency-domain response in resonant status. The inductance and capacitance measurement accuracy of the proposed method is validated by COMSOL simulation through the proposed virtual vector network analyzer (VNA). Then, experimental results show that the inductance measuring by the proposed method holds exactly consistent with commercial instruments, whose error is as less as 3%. Each parameter (rather than partial parameters) of the ECT sensor topology circuit can be identified by the proposed method. Compared to traditional ECT sensors, the proposed method provides additional parameters as capacitance value in characterizing both winding capacitance and coaxial cable capacitance and resistance value characterizing conductivity variations due to crack or stress. Moreover, multiparameter evaluation provides the possibility for parameter fusion, and the signal-to-noise ratio (SNR) or sensitivity of ECT sensors in crack detection can be significantly improved.**

***Index Terms*— Capacitance measurement, eddy current (ECT) sensor, inductance measurement, inductive sensor.**

## I. Introduction

RESONANT inductive circuit has been applied in a lot of fields. It has been reported in eddy current (ECT) sensor [1], nuclear magnetic resonance [2], power system [3], and so on. Inductive sensor [4] has developed from single parameter to multiparameter sensing. Yu *et al.* [5] invert inductance and resistance through amplitude and phase, and multiparameters are used for parameter fusion. Shi *et al.* [6] detect metal debris in oil from the inductance and resistance variation of coil probe. In addition, the capacitance of the sensor needs to be identified [7]. Yin *et al.* [8] detect metallic structures defects though both the inductance and stray capacitance of the planar coil. Capacitance includes coaxial capacitance [9] and winding capacitance [10]. It is parallel [3] with inductance and resistance. This poses a challenge to the multiparameter identification of inductive sensor.

*LCR* meter is the customary method for inductance [11] or capacitance [12] measurement. Cho [13] uses a multifrequency *LCR* meter to measure the inductance of delay lines and characterize the inductance variation due to temperature and bias current. Shi and Chung [12] used an *LCR* meter to measure capacitance and realize nondestructive evaluation of steels. *LCR* meter is mostly used in kilohertz [14], [15]. Impedance analyzer [16] and vector network analyzer (VNA) [17] for resistance and inductance measurement have been reported in high-frequency applications.

Otherwise, measurement methods without large-scale instruments have also been reported. Waltrip and Seifert [11] used an external programmable capacitor to calculate the inductance and capacitance through the impedance value under different capacitors. To avoid external devices calibration, Masilamany *et al.* [18] adopted multifrequency point measurement and curve fitting to measure inductance and resistance values. De Angelis *et al.* [7] used impedance model formula to invert *LC* parameters.

Inductive sensor, especially ECT sensor, requires not only inductance and resistance measurement but also capacitance measurement. Therefore, it is necessary to study the measurement method integrating the advantages of the above methods. This method should meet the conditions of no external standard devices, inductance resistance capacitance simultaneous measurement, broadband applicability, and so on.

Consequently, a method for measuring each parameter of the ECT sensor electrical topology circuit with high frequency is proposed in this article. This method converts inductance, capacitance, and resistance into a function of frequency, and the frequency is calibrated by the commercial instrument itself, so calibration devices other than the instrument itself can be omitted.

## II. Methodology

The proposed method of inductive sensor multiparameters identification is based on the technology of piezoelectric crystal parameters measurement. This method builds on the

Manuscript received February 14, 2022; revised April 14, 2022; accepted May 4, 2022. Date of publication May 27, 2022; date of current version June 21, 2022. This work was supported in part by the National Natural Science Foundation of China under Grant 61701085, in part by the Department of Science and Technology of Sichuan Province under Grant 2019JDZH0020, and in part by the Key Laboratory of Nondestructive Testing of Fujian Polytechnic Normal University under Grant S2-KF2013. The Associate Editor coordinating the review process was Dr. Roman Sotner. *(Corresponding author: Dong Liu.)*

Dong Liu, Qiuping Ma, Haoran Li, and Bin Gao are with the School of Automation Engineering, University of Electronic Science and Technology of China, Chengdu, Sichuan 611731, China (e-mail: dong.liu@uestc.edu.cn; mqp@std.uestc.edu.cn; horn_lee@std.uestc.edu.cn; bin_gao@uestc.edu.cn).

Hong Zhang is with the Key Laboratory of Non-Destructive Testing Technology, Fujian Polytechnic Normal University, Fuzhou, Fujian 350300, China (e-mail: zhhgw@hotmail.com).

Xiaoting Xiao is with the School of Electrical Engineering and Information, Southwest Petroleum University, Chengdu, Sichuan 610599, China (e-mail: xiaoting.xiao@swpu.edu.cn).

Guiyun Tian is with the School of Engineering, Newcastle University, Newcastle upon Tyne, U.K. (e-mail: g.y.tian@ncl.ac.uk).

Jianbo Wu is with the School of Engineering, Sichuan University, Chengdu, Sichuan 610054, China (e-mail: wujianbo@scu.edu.cn).

Digital Object Identifier 10.1109/TIM.2022.3178493

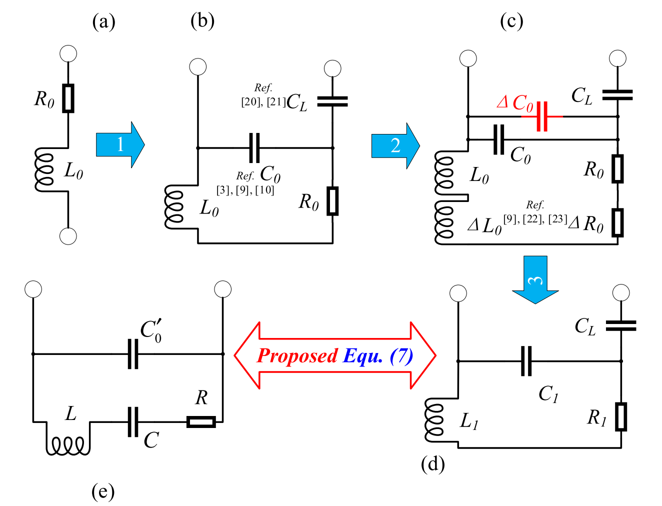


Fig. 1. Evolution of ECT sensor electrical topology. (a) Coil. (b) Coil with winding, coaxial, and grounding capacitance. (c) Coil close to metal. (d) Simplified model of coil close to metal. (e) Piezoelectric crystal BVD model.

equivalent conversion between the ECT sensor topology circuit and the piezoelectric crystal topology circuit.

There are two reasons why piezoelectric crystal and its equivalent conversion are selected. First, piezoelectric crystal parameters extraction method obtains the parameters in the state of resonance. Therefore, the ECT sensor multiparameters separation can be realized in resonant states. Considering that ECT sensor has higher defect sensitivity or signal-to-noise ratio (SNR) in the resonant state [9], ECT sensor parameters separation in resonant states may bring some benefits to defect sensitivity or SNR. Second, the piezoelectric crystal parameter extraction method can extract all of the four parameters. Correspondingly, the ECT sensor parameters measurement method based on the piezoelectric crystal and its equivalent transformation can realize parameters measurement not only inductance and resistance, but also capacitance, even grounding capacitance. More parameters of ECT sensor are convenient to characterize more sensor characteristics and realize multiphysical separation or fusion. In conclusion, the ECT sensor parameters measurement method based on the piezoelectric crystal and its equivalent transformation can realize multiparameters measurement in resonant states.

In this section, the electrical topology evolution of the ECT sensor will be introduced first. Second, the equivalent conversion between the ECT sensor topology circuit and piezoelectric crystal topology circuit will be derived. Third, a method of measuring each parameter of ECT sensor electrical topology is proposed.

### A. ECT Sensor Electrical Topology Evolution

ECT sensor is generally considered to have a topology circuit [19], as shown in Fig. 1(a). In this model, inductance $L_0$ represents the coil inductance and $R_0$ represents coil energy loss [20].

Considering winding capacitance [3], [10], coaxial cable capacitance [9], and grounding capacitance [20], the ECT sensor has the topology circuit, as shown in Fig. 1(b), where $C_L$ represents the grounding capacitance and $C_0$ was considered as the capacitive coupling between turns (winding capacitance) [3] and coaxial cable capacitance [9].

Otherwise, the resonant circuit of capacitor in series with coil is often reported [21]. In this condition, $C_L$ also contains the capacitance of series capacitor.

When the ECT sensor is in close proximity to a metal surface, the induced ECT has a mutual inductance with the coil, which has been included in the circuit topology, as shown in Fig. 1(c). $\Delta L_0$ and $\Delta R_0$ are the variations of $R_0$ and $L_0$ caused by inductance mutual [9], [22], [23], and there are

$$\Delta R_0 = \frac{1}{2}\omega R_0 k^2 \tag{1}$$

$$\Delta L_0 = -\frac{1}{2}L_0 k^2 \tag{2}$$

where $k$ is the coefficient of inductance mutual.

The study in this article shows that: $\Delta C_0$ consists of two parts: coaxial cable length change and winding capacitance variation caused by metal proximity.

Fig. 1(c) can be simplified to Fig. 1(d), and there are $L_1 = L_0 + \Delta L_0$, $R_1 = R_0 + \Delta R_0$, and $C_1 = C_0 + \Delta C_0$.

Fig. 1(e) is the electrical topology circuit of a piezoelectric crystal. It is named Butterworth-Van Dyke (BVD) model [24]. The BVD model has been widely studied. If the relationship between Fig. 1(d) and (e) can be demonstrated, the technology in the piezoelectric field can be transplanted to the ECT sensor. Our studies have shown the existence of this equivalent transformation [25]. This equivalent transformation builds a bridge between piezoelectric crystal and ECT sensor.

Then, let us introduce the derivation of the equivalent conversion.

### B. Proposed Equivalent Transformation Between ECT Sensor Electrical Topology and BVD Model

If two electrical topology circuits are equivalent, the impedance of those two electrical topology circuits is equal in any frequency [24].

The impedance of the ECT sensor in Fig. 1(d) is calculated by

$$Z(\omega) = \frac{(R_1 + j\omega L_1)/j\omega C_1}{(R_1 + j\omega L_1) + 1/j\omega C_1} + \frac{1}{j\omega C_L}. \tag{3}$$

The impedance of the BVD model in Fig. 1(e) is expressed as

$$Z'(\omega) = \frac{1 - \omega^2 LC + j\omega RC}{\left(1 - \omega^2 LC + j\omega RC\right) j\omega C_0' + j\omega C}. \tag{4}$$

If there is an equivalent transformation between these two electrical topology circuits, then $Z(\omega) = Z'(\omega)$ for any frequency [24], namely

$$\frac{(R_1 + j\omega L_1)/j\omega C_1}{(R_1 + j\omega L_1) + 1/j\omega C_1} + \frac{1}{j\omega C_L} = \frac{1 - \omega^2 LC + j\omega RC}{\left(1 - \omega^2 LC + j\omega RC\right) j\omega C_0' + j\omega C}. \tag{5}$$

By simplifying formula (5) and grouping the similar items in the same order of $\omega$, the equation is presented as

$$\begin{aligned}
&j\omega^5\{LCC_0'(L_1C_L+L_1C_1)-L_1C_1C_LLC\}\\
&\quad+\omega^4\begin{Bmatrix}LCC_0'(R_1C_L+R_1C_1)-L_1C_1C_LRC\\+RCC_0'(L_1C_L+L_1C_1)-R_1C_1C_LLC\end{Bmatrix}\\
&\quad-j\omega^3\begin{Bmatrix}LCC_0'+RCC_0'(R_1C_L+R_1C_1)+\\(C+C_0')(L_1C_L+L_1C_1)-L_1C_1C_L\\-C_LLC-R_1C_1C_LRC\end{Bmatrix}\\
&\quad-\omega^2\begin{Bmatrix}RCC_0'+(C+C_0')(R_1C_L+R_1C_1)\\-R_1C_1C_L-C_LRC\end{Bmatrix}\\
&\quad+j\omega\{(C+C_0')-C_L\}=0.
\end{aligned}\tag{6}$$

Because $Z(\omega)=Z'(\omega)$ holds for arbitrary $\omega$, coefficients with the same order of $\omega$ in the left side of formula (4) must be equal to zero [24]. That is, the expression in each brace of formula (4) is equal to zero. Thus, five equations can be established. Then, it can be simplified and namely

$$\begin{cases}C_L=C+C_0'\\C_1=C_0'(1+C_0'/C)\\R_1=RC^2/(C+C_0')^2\\L_1=LC^2/(C+C_0')^2.\end{cases}\tag{7}$$

From (7), the proposed equivalent transformation is obtained. Although this equivalent transformation, the electrical technology in the piezoelectric crystal can be applied to the ECT sensor field. Next, we will specify the ECT sensor parameters identification though piezoelectric technology.

### *C. Self-Resonance Multiparameters Identification for ECT Sensor*

The parameters measurement method of BVD model though VNA has been studied in our previous works [26], [27]. Although the proposed equivalent transformation in (7), this method can be transferred to the ECT sensor. The proposed method of ECT sensor multiparameters identification is as follows.

*1) ECT Sensor Frequency Response:* The ECT sensor frequency response data can be obtained through instrument as VNA. The block diagram of parameters measurement system is shown in Fig. 2.

ECT sensors are connected to the instrument through a fixture. $R_m$ is the measuring resistance, and it is usually 50, 75, or 100 Ω. $R_r$ is the internal resistance of the test system. The ac is a variable frequency source. $C_L$ represents the grounding capacitance, and $L_1$, $R_1$, and $C_1$ are the inductance, resistance, and capacitance of the ECT sensor.

VNA operates in sweep mode and obtain the scattering ($S$-)parameters of the ECT sensor in resonance. It namely the frequency response curve of forwarding transmission coefficient ($S_{21}$). This frequency response curve contains two parts: the phase frequency response curve of the forward transmission coefficient $\mathrm{Phase}_{\mathrm{measure}}(S_{21})$ and the magnitude frequency response curve of the forward transmission coefficient $\mathrm{Mag}_{\mathrm{measure}}(S_{21})$.

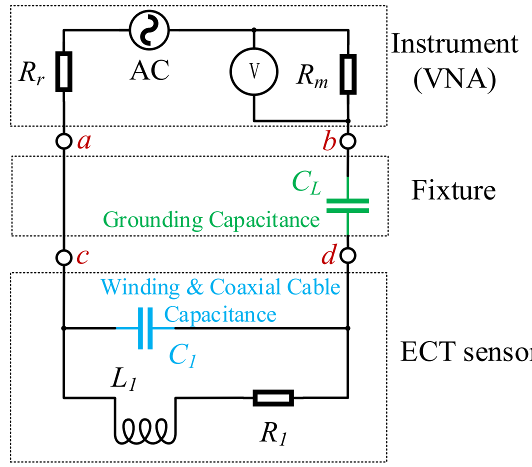


Fig. 2. Measurement system diagram of ECT sensor topological circuit parameters identification.

Although the phase frequency response curve $\mathrm{Phase}_{\mathrm{measure}}(S_{21})$, four features value can be extracted: $f_r$, $f_a$, $\Delta_1$, and $\Delta_2$ [26]. Those features are defined as: resonance frequency ($f_r$), antiresonance frequency ($f_a$), the slope of phase frequency response curve at $f_r$ ($\Delta_1$), and the slope of phase frequency response curve at $f_a$ ($\Delta_2$).

Although the magnitude frequency response curve $\mathrm{Mag}_{\mathrm{measure}}(S_{21})$, two features value can be extracted: $\mathrm{Max}[\mathrm{Mag}_{\mathrm{measure}}(S_{21})]$ and $f_{\max}$ [27]. Those features are defined as: maximum value of the magnitude frequency response curve ($\mathrm{Max}[\mathrm{Mag}_{\mathrm{measure}}(S_{21})]$) and the frequency corresponding to the maximum point of the magnitude frequency response curve ($f_{\max}$).

*2) BVD Model Parameters:* The equivalence of ECT sensor electrical topology and piezoelectric crystal BVD model has been proven. Therefore, they have the same $\mathrm{Phase}_{\mathrm{measure}}(S_{21})$ and $\mathrm{Mag}_{\mathrm{measure}}(S_{21})$. Moreover, they have the same $f_r$, $f_a$, $\Delta_1$, $\Delta_2$, $\mathrm{Max}[\mathrm{Mag}_{\mathrm{measure}}(S_{21})]$, and $f_{\max}$.

Bring the above six parameters into formula (8), the parameters of the BVD model can be obtained

$$\begin{cases}\dfrac{(2\pi f_a)^2+(2\pi f_r)^2}{2}=\dfrac{1}{LC}+\dfrac{1}{2LC_0'}-\dfrac{R^2}{2L^2}\\(2\pi f_r)^2(2\pi f_a)^2=\dfrac{1}{L^2C^2}\left(1+\dfrac{C}{C_0'}\right)\\\Delta_1=\left.\dfrac{\partial(\mathrm{Phase}(S_{21}))}{\partial f}\right|_{f=f_r}\\\Delta_2=\left.\dfrac{\partial(\mathrm{Phase}(S_{21}))}{\partial f}\right|_{f=f_a}\\\mathrm{Max}\left[\mathrm{Mag}_{\mathrm{measure}}(S_{21})\right]=\mathrm{abs}(G(f_{\max}))\end{cases}\tag{8}$$

where $\mathrm{Phase}(S_{21})$ is defined as [26]

$$\mathrm{Phase}(S_{21})=\frac{180}{\pi}\mathrm{atan}\left(\frac{\mathrm{imag}(G(f))}{\mathrm{real}(G(f))}\right).\tag{9}$$

$G(f)$ is the ratio of the vector voltage on the measuring resistance $R_m$ to the vector voltage of the ac signal source. It was defined as

$$G(f)=\frac{U_m}{U}=\frac{R_m}{Z'(f)+R_r+R_m}.\tag{10}$$

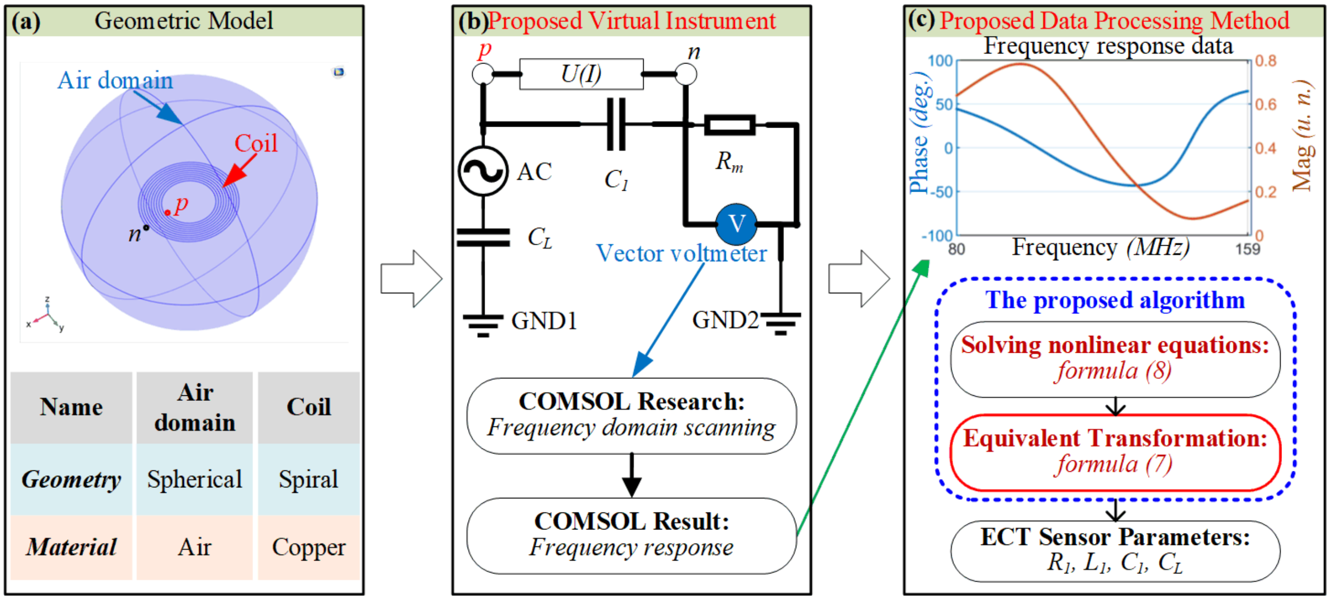


Fig. 3. Schematic of simulation verification. (a) Geometric model. (b) Proposed virtual instrument. (c) Proposed data processing method.

$Z'(f)$ is the impedance of the BVD model in Fig. 1(e). It was defined in formula (4).

abs($G(f)$) is the magnitude of the complex number $G(f)$.

By solving the partial differential equations formula (8) through the finite element numerical solution method [27], we can obtain the BVD model parameters: $R$, $L$, $C$, and $C_0'$.

*3) ECT Sensor Parameters:* The conversion between the BVD model parameters and the ECT sensor parameters can be realized through the proposed conversion in formula (7). By bringing the BVD model parameters ($R$, $L$, $C$, and $C_0'$) into formula (7), the ECT parameters ($R_1$, $L_1$, $C_1$, and $C_L$) can be obtained.

This method separates not only $R_1$ and $L_1$ but also capacitance $C_1$. Thus, self-resonance *LCR* parameters identification of ECT sensors can be realized.

## III. Proposed COMSOL Virtual Instrument and Simulation Verification

The proposed method can be verified through the COMSOL simulation. This simulation contains three steps: 1) coil geometric model construction; 2) COMSOL virtual instrument proposal; and 3) virtual instrument measurement data processing though the proposed method.

The schematic of the COMSOL simulation is shown in Fig. 3. The specific steps are illustrated as follows.

### A. Coil Geometric Model Construction

The coil is generated by the COMSOL spiral tool. The material of the coil is copper. The coil is wrapped in spherical air. It is shown in Fig. 3(a). The geometric parameters of the coil are shown in Table I.

In Table I, the parameters are defined as, $N$: the number of windings of the coil, $W$: linewidth of coil, $S$: line space of coil, $H$: line height of coil, $D$i: inner diameter, and $D$o: outer diameter.

TABLE I
Coil Geometric Parameters in Simulation

| Name | N(*turn*) | W(*um*) | S(*um*) | H(*um*) | Di(*mm*) | Do(*mm*) |
|---|---|---|---|---|---|---|
| Value | 13 | 152.40 | 152.40 | 34.29 | 2.44 | 10.36 |

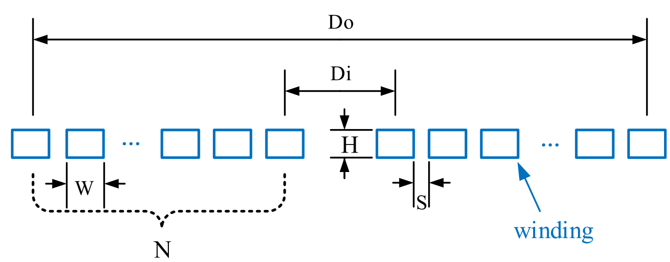


Fig. 4. Schematic of coil parameters.

The schematic of coil geometric parameters is shown in Fig. 4.

### B. COMSOL Virtual Instrument Proposal

In this article, a virtual instrument equivalent to VNA is proposed. It was constructed through COMSOL ac/dc module. The circuit structure of the virtual instrument is shown in Fig. 3(b). The coil is connected to the ac/dc module through point "p" and point "n." Its electrical response is represented by COMSOL's "external U versus I" module.

The device in Fig. 3(b) is define as, $C_L$: grounding capacitance, where $C_L = 20$ pF; $C_1$: includes winding capacitance and coaxial capacitance, where $C_1 = 10$ pF; $R_{\mathrm{m}}$: measuring resistance, where $R_{\mathrm{m}} = 100\ \Omega$; ac: variable frequency source, where the amplitude is 1 V; GND: grounding lead; and $V$: vector voltmeter.

The research of COMSOL simulation contains two steps.

1) Coil geometry analysis module. To obtain "U versus I" response of coil under specific geometry.

TABLE II
SET AND CALCULATED PARAMETERS IN SIMULATION

| Parameters | $R_1(\Omega)$ | $L_1(uH)$ | $C_1(pF)$ | $C_L(pF)$ |
|---|---|---|---|---|
| Set | Null | 0.99 | 10.00 | 20.00 |
| Calculated | 19.55 | 0.96 | 9.89 | 20.11 |

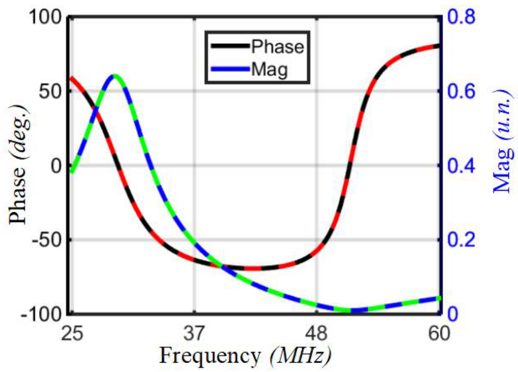


Fig. 5. Simulation curve and calculation parameter inversion curve.

2) Frequency domain analysis. Change the output frequency of ac.

Then, the frequency response of the coil can be recorded through the vector voltmeter.

### C. Virtual Instrument Measurement Data Processing Through the Proposed Method

Simulation data processing contains three steps.

1) The data obtaining by the vector voltmeter are converted into the phase frequency response curve and the magnitude frequency response curve.
2) Obtain BVD model parameters through formula (8).
3) Obtain ECT sensor parameters through formula (7).

The parameters calculated through the above steps are shown in Table II. We input the geometric parameters in Table I into the Texas Instrument coil designer tool. The inductance value calculated by the Texas Instrument coil designer tool is 0.99 $\mu$H. It is called set inductance value in Table II. This value is taken as the standard value and compared with the inductance value calculated by the simulation. The website of the tool is: https://webench.ti.com/wb5/LDC/#/spirals.

Comparing the set and calculated parameters in Table II, it can be found that the measurement error of capacitance and inductance are is than 1.10% and 3.03% separately.

The small errors shown in Table II have confirmed the accuracy of the proposed method. Moreover, the curve of the calculated parameters inversion further shows the accuracy of this method. The curve obtained by simulation is shown in Fig. 5 as marked with the solid line. The calculated parameters inversion curve is shown in Fig. 5 as marked in dotted line. For the phase frequency response curve, the root mean square (rms) error between the solid line and dotted line is 0.04. For the magnitude frequency response curve, it is $0.19 \times 10^{-2}$. The coincidence between the solid line and the dotted line is high, which indirectly proves the accuracy of parameter extraction.

Simulation results have verified the accuracy of the method. The accuracy of the proposed method will be further demonstrated in Section IV by experiments.

## IV. EXPERIMENT PLATFORM AND SAMPLES

The experiments of this article consist of three parts. First, the inductance measuring by the proposed method will be compared with the inductance measuring by impedance analyzer and *LCR* meter. Therefore, the measurement accuracy of inductance will be verified. Second, the parameter of ECT sensor under different lengths of coaxial cable will be measured. Thus, the ability of the proposed method to separate coaxial cable capacitance will be verified. Finally, a metal crack will be imaged by multiparameters fusion though mechanical arm C-scan. Consequently, the potential value of multiparameter measurement will be preliminarily demonstrated.

### A. Experiment Platform

The block diagram and actual photographic of the experimental system are shown in Fig. 6. The mechanical arm is used to realize the C-scan. In particular, the frequency response data in each position can be obtained from the VNA.

The specific experimental steps are as follows.

First, the PC controls the mechanical arm to scan the specimen point by point. The step of each point is 1 mm $\times$ 2 mm. The resolution of the scan is 31 $\times$ 26. The total scanning point is 806 points.

Second, the PC writes the control parameters into the instrument remotely through the client. The control parameters contain frequency band, intermediate frequency bandwidth (IFBW), power level, and so on. Then, the frequency response data can be obtained.

Third, the frequency response data will be processed by the proposed method and the multiparameters will be obtained.

Finally, the parameters will be fused after physical analysis for the purpose of improve sensitivity or SNR. The potential value of multiparameter measurement will be preliminarily demonstrated.

The uncertainty source of the experimental system includes three parts: $Z$-axis displacement error of mechanical arm, electronic noise of the VNA, and parameter calculation error of formula (8). Through COMSOL simulation data calculation, the error of the parameter calculation error of formula (8) is 1.10%. Take the measurement result of impedance analyzer as the standard value, there exists approximately 40% of the error comes from the calculation method and 60% from the instrument noise as well as the jitter of mechanical system. Compared with the instrument output ($-0.\ x$ dB), the rms error (0.002 dB) is small. Thus, mechanical jitter may be the main factor caused the rest 60% error.

### B. Samples

Two kinds of sensors are used in the experiments, namely, printed circuit board (PCB) coil and flexible coil. Compared

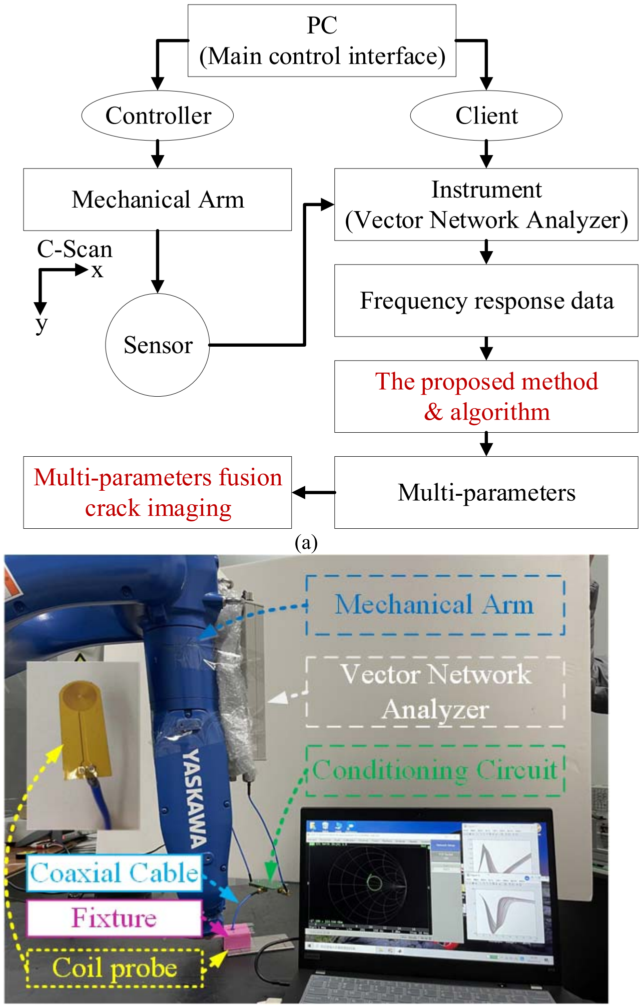


Fig. 6. (a) Block diagram and (b) actual photographic of the experimental system.

with PCB coil, flexible coil cannot avoid inductance error caused by micro deformation in transports. Therefore, PCB coils are selected and transported to other laboratories, and their inductance will be measured by large-scale instruments impedance analyzer HIOKI IM3570 in $L_S$ frequency scanning method. The measurement results will be compared with the results measured by the proposed method. Compared with PCB coil, flexible coil has narrower linewidth and higher turns. Therefore, a flexible coil in commercial polyurethane is adopted for sensor application.

In order to demonstrate the ability of the proposed method to identify the capacitance of coaxial cable, coil with different lengths of coaxial cable is adopted. The lengths are 5, 15, and 25 cm, respectively.

In order to demonstrate the parameters variation when the ECT sensor close to the metal, a steel metal specimen with artificial defect is adopted.

*1) Sensors:* The actual photographic of the PCB coil and flexible coil is shown in Fig. 7.

For comparison, the geometric parameters of PCB coil are consistent with the simulation setting. The flexible coil has the approximate outer diameter with PCB coil. Flexible coil

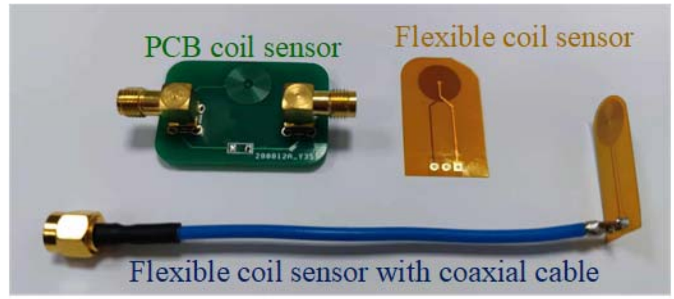


Fig. 7. Actual photographic of coil probe.

TABLE III
FLEXIBLE COIL GEOMETRIC PARAMETERS

| Name | N(*turns*) | W(*um*) | S(*um*) | H(*um*) | Di(*mm*) | Do(*mm*) |
|---|---|---|---|---|---|---|
| Flexible Coil | 37 | 60 | 60 | 200 | 1.2 | 10 |

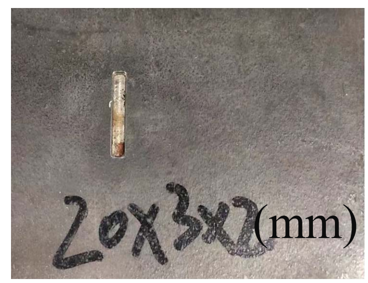


Fig. 8. Metal specimen.

probe is manufactured with lithography process, and smaller linewidth can be achieved. Narrow linewidth provides higher turns in the same area of the sensor. More turns provide greater inductance and higher sensing sensitivity. The geometric parameters of the flexible coil are shown in Table III.

Two types of flexible coils are used in the experiment. There are single-layer coil and double-layer coil. So as to display the parameter changes caused by the number of layers.

*2) Metal Specimen:* The steel specimen with artificial defect is shown in Fig. 8. The size of the artificial defect is 20 mm × 3 mm × 2 mm (length × width × depth).

## V. RESULTS AND DISCUSSION

In this part, we first compared the inductance of PCB coil measured by the proposed method, impedance analyzer and *LCR* meter, separately. The measurement error of the proposed method relative to impedance analyzer is discussed.

Second, the measured parameters of single-layer flexible coil probe with different coaxial cable lengths are compared. The variation of capacitance, resonance frequency, and resistance causing by the change of coaxial cable lengths is discussed. Thus, the capacity of the proposed method to separate the inductance and capacitance without destroying the resonant state is verified.

Finally, the crack in a steel is visualized by the proposed multiparameters measurement method. The sensitivity

TABLE IV
COMPARISON OF INDUCTANCE MEASURED BY DIFFERENT METHODS

| Method | The proposed method | Impedance analyzer | LCR meter |
|---|---|---|---|
| $L_1(uH)$ | 1.01 | 0.98 | 0.86 |

TABLE V
PARAMETERS OF SINGLE-LAYER FLEXIBLE COIL PROBE WITH DIFFERENT COAXIAL CABLE LENGTHS

| Name | Parameters value | | | STD error |
|---|---|---|---|---|
| Coaxial cable length(cm) | 5 | 15 | 25 | Null |
| $R_1$ (Ω) | 21.86 | 18.77 | 17.58 | 2.21 |
| $L_1$ (uH) | 3.08 | 3.12 | 3.11 | 0.02 |
| $C_1$ (pF) | 27.97 | 39.38 | 48.24 | 10.16 |
| $C_L$ (pF) | 100.13 | 101.54 | 103.61 | 1.75 |

of parameters is analyzed, and a parameter fusion scheme is given to further improve the sensitivity

### *A. Inductance Measurement Comparing With Impedance Analyzer and LCR Meter*

The inductances of PCB coil measured by the impedance analyzer and *LCR* meter are 0.98 and 0.86 $\mu$H, respectively.

The impedance analyzer used in Table IV is HIOKI IM3570. The resolution and accuracy of HIOKI IM3570 are 0.000001 $\mu$H and $\pm 0.08\%$ rdg., respectively. The screenshot of the experiment is shown in Fig. 9(a). The *LCR* meter is Tonghui TH2830. It was supplied by Changzhou Tonghui Electronic Company Ltd., Changzhou, China. The resolution and accuracy of Tonghui TH2830 are 0.00001 $\mu$H and 0.1% rdg., respectively. The photograph of the experiment is shown in Fig. 9(b).

The parameters measured by the proposed method are: $R_1 = 2.10$ Ω, $L_1 = 1.01$ $\mu$H, $C_1 = 10.41$ pF, and $C_L = 40.26$ pF. The comparison of the inductance measured by different methods is shown in Table IV. Compared with impedance analyzer, the inductance error measured by the proposed method is as less as 3%.

### *B. L&C Identification and Coaxial Cable Length Separation*

The parameters of single-layer flexible coil probe with different coaxial cable lengths are shown in Table V. It is measured by the proposed method.

It can be seen from Table V that the resistance, capacitance, and resonant frequency change greatly with the variation of coaxial cable lengths. However, the inductance does not change with the variation of coaxial cable lengths. The standard deviation (STD) of inductance measurement is as low as 0.02. This shows that the inductance measurement of the proposed method is not disturbed by coaxial cable lengths. Thus, the ability of L&C identification and separation can be verified.

The relationship between capacitance and coaxial cable lengths is shown in Fig. 10. The *R*-square between measured

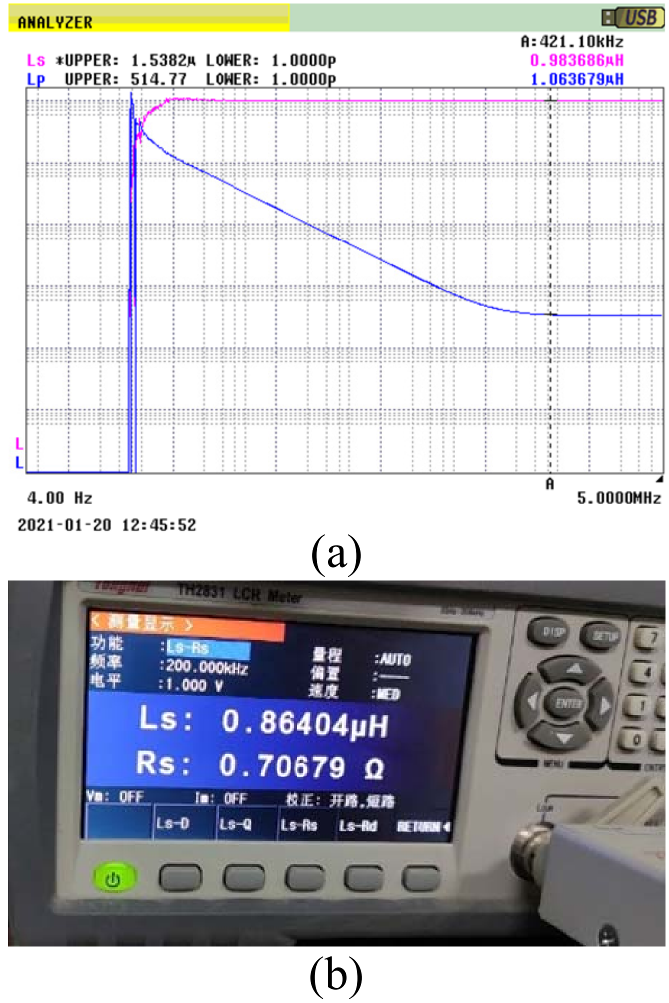


Fig. 9. Parameters measured by commercial instruments. (a) Measured by impedance analyzer. (b) Measured by *LCR* meter.

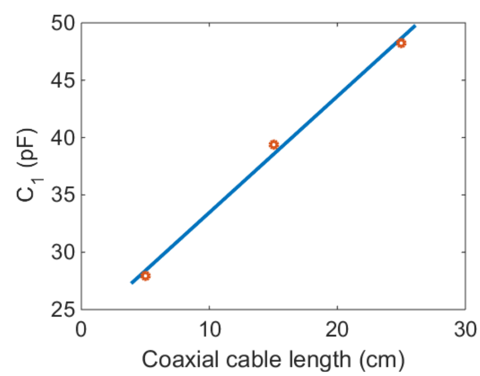


Fig. 10. Capacitance measured under different coaxial cable lengths.

points and fitting line is as high as 0.99, which indicated the high linearity between measured capacitance and wire length. Thus, this indirectly verifies the accuracy of capacitance measurement.

Because the capacitance varies with the length of the conductor, the resonance frequency varies with the capacitance. Finally, the resonance frequency variation leads to the variation of current skin depth. As a result, the resistance has changed.

In conclusion, this method can measure the absolute value of inductance. The STD of inductance measurement caused by coaxial cables capacitance variation is as low as 0.02. This method weakened the interference of the variation of coaxial cables length. It has potential benefits for the sensors with different lengths of lead wire, such as planar sensor array.

### C. Metal Crack Imaging

The metal crack imaging experiment is divided into two steps. First, the crack is imaged by various parameters. The SNR of parameters to crack imaging will be discussed. Then, two parameters fusion methods are discussed to improve the SNR or sensitivity.

*1) Metal Crack Imaging in Different Parameters:* At the point above the crack, the parameters measured by double-layer flexible coil are: $R_1 = 64.83\ \Omega$, $L_1 = 5.67\ \mu$H, $C_1 = 28.84$ pF, and $C_L = 101.85$ pF. Compared with the parameters of single-layer flexible coil in Table V, double-layer flexible coil has more turns and higher inductance. More turns are beneficial to the sensitivity of the sensor, while the double-layer flexible coil is adopted to image the metal crack.

The imaging results of steel specimen with artificial defect are shown in Fig. 11. The crack is separately imaged by resistance ($R_1$), inductance ($L_1$), winding capacitance ($C_1$), and grounding capacitance ($C_L$). In order to observe the SNR of crack imaging, we draw the image in 3-D. The $X$ and $Y$ coordinates represent the sensor's position, and the $Z$ coordinate represents the parameter value. In order to observe the accuracy of crack location judgment, we describe the measured data with contour lines and mark the location of the crack with a red box.

In Fig. 11, it can be found that the resistance ($R_1$) and inductance ($L_1$) have a visible SNR to identify crack. At the crack location, the contour line forms an obvious loop. For winding capacitance ($C_1$), it also has a perception of crack, but the SNR decreases. However, the grounding capacitance scarcely has SNR to the crack.

For comparison in numerically, the definition of SNR should be calibrated first and discussed. SNR has been defined as the ratio of signal in defective regions and nondefective regions [28]. So, the difference between average value in crack and noncrack regions should be considered as signal. However, the noise of the sensor itself should be considered. This noise has been evaluated by the rms [29]. Therefore, the STD is used to evaluate the noise. Refer to the colleagues' research [28], [29], the SNR in this article is defined as

$$\mathrm{SNR} = 20\log_{10}\left(\frac{\mathrm{mean}(P_{\mathrm{Crack}}) - \mathrm{mean}(P_{\mathrm{NoCrack}})}{\mathrm{STD}(P_{\mathrm{NoCrack}})}\right) \quad (11)$$

where $\mathrm{mean}(P_{\mathrm{Crack}})$ and $\mathrm{mean}(P_{\mathrm{NoCrack}})$ are the parameters' average values in crack and noncrack regions, respectively, and $\mathrm{STD}(P_{\mathrm{NoCrack}})$ is the STD of parameters in noncrack regions.

Finally, the SNRs of all parameters are shown in Table VI.

From Table VI, it can be found that crack can be imaged by not only the resistance and inductance but also the winding capacitance. Although the SNR of the winding capacitance is decreases, it still has about half of the inductance's SNR.

TABLE VI
SNR OF PARAMETERS

| Parameters | $R_1$ | $L_1$ | $C_1$ | $C_L$ |
|---|---|---|---|---|
| SNR (*dB*) | 15.50 | 18.72 | 8.42 | 3.25 |

TABLE VII
SNR AND SENSITIVITY OF FREQUENCY

| Parameters | $f_r$ | $f_s$ |
|---|---|---|
| SNR (*dB*) | 20.79 | 20.23 |
| Sensitivity (*MHz*) | 0.64 | 1.44 |

Fig. 11(c) also supports this numerical result. Most colleagues ignore the variation of winding capacitance. However, this experiment shows that when the lift-off is 0.2 mm, the variation of winding capacitance can also characterize the defects, and the proposed method provides a scheme for measuring not only the variation of resistance and inductance but also the variation of the winding capacitance.

*2) Metal Crack Imaging in Parameters Fusion:* For the ECT sensor, the SNR or sensitivity maybe improved through parameters fusion.

The resonant frequency ($f_{\mathrm{r}}$) is the fusion information including resistance, inductance winding capacitance, and grounding capacitance. Therefore, the resonance frequency is used to image the crack. The crack imaged by resonance frequency is shown in Fig. 12(a). Compared to the contour line in Fig. 11, there is a more obvious loop in Fig. 12(a), and the SNR maybe higher.

The product of $LC$ has been used as a fusion feature parameter [7]. Further analysis of Fig. 11, it can be found that $L_1$ and $C_1$ have increased in the crack regions. The mean values of $L_1$ in nondefective regions and defective regions are 4.69 and 5.46 $\mu$H, respectively. The mean values of $C_1$ in nondefective regions and defective regions are 26.89 and 28.63 pF, respectively. However, $R_1$ decreases in the crack regions, which contrary to the variation of $L_1$ and $C_1$. Relative to resonant frequency, the product of $L_1$ and $C_1$ does not contain $R_1$ and may have higher sensitivity.

In order to compare with the resonant frequency, we convert the product of $L_1$ and $C_1$ into the form of frequency. Referring to the definition of series resonant frequency ($f_{\mathrm{s}}$) in quartz crystal [30], the new frequency is fused as

$$f_{\mathrm{s}} = \sqrt{\frac{1}{L_1 C_1}}. \quad (12)$$

The crack imaged by $f_{\mathrm{s}}$ is shown in Fig. 12(b). The comparison of SNR and sensitivity of those two frequencies is shown in Table VII. Sensitivity is the difference value of the mean frequency between the nondefective region and defective region.

Table VII shows that the SNR of the fused parameters is significantly improved. The SNR has been increased by 2–12 dB. Table VII also shows the difference of sensitivity in different fusion methods. When the parameters are fused to $f_{\mathrm{s}}$, the frequency variation has increased more than 200%.

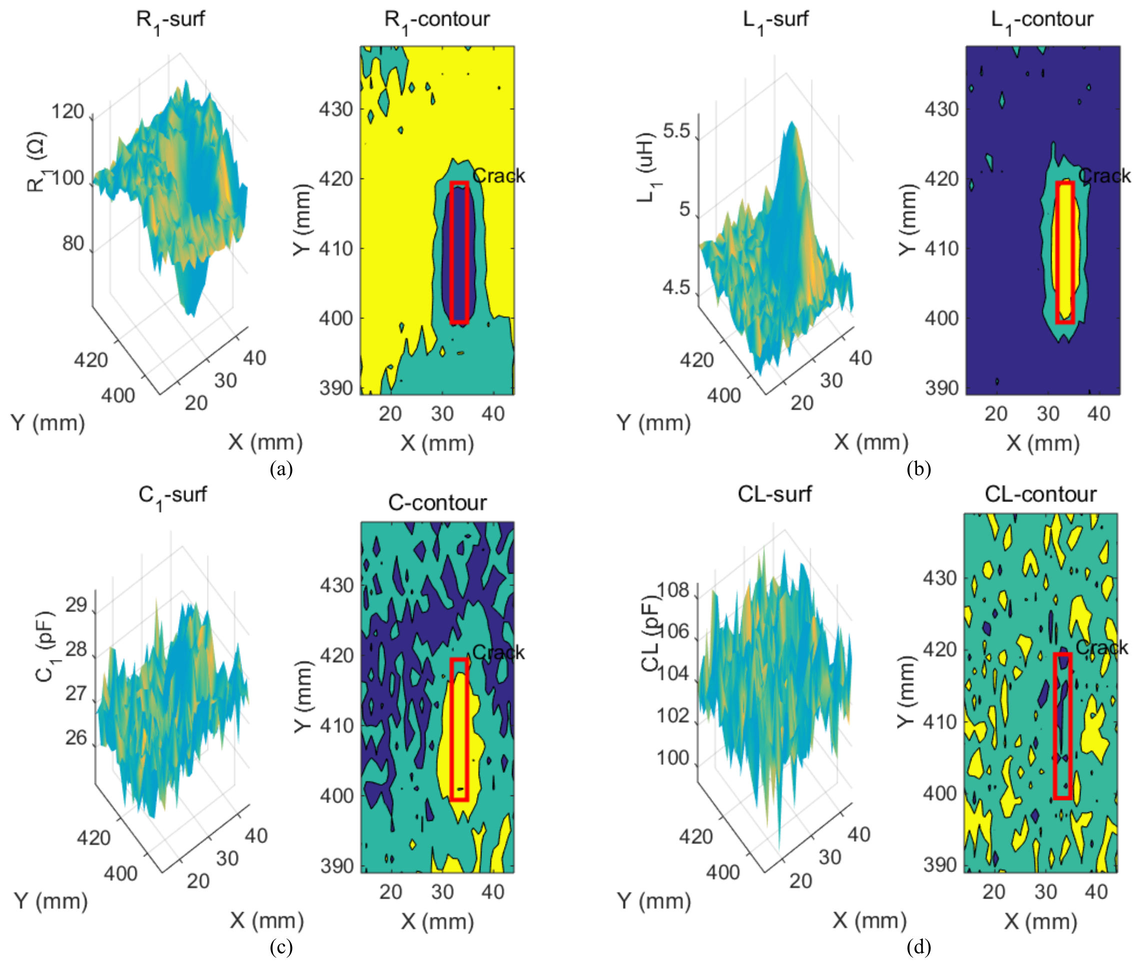


Fig. 11. Steel artificial defect imaged by different ECT sensor parameters. (a) Resistance ($R_1$). (b) Inductance ($L_1$). (c) Winding capacitance ($C_1$). (d) Grounding capacitance ($C_L$).

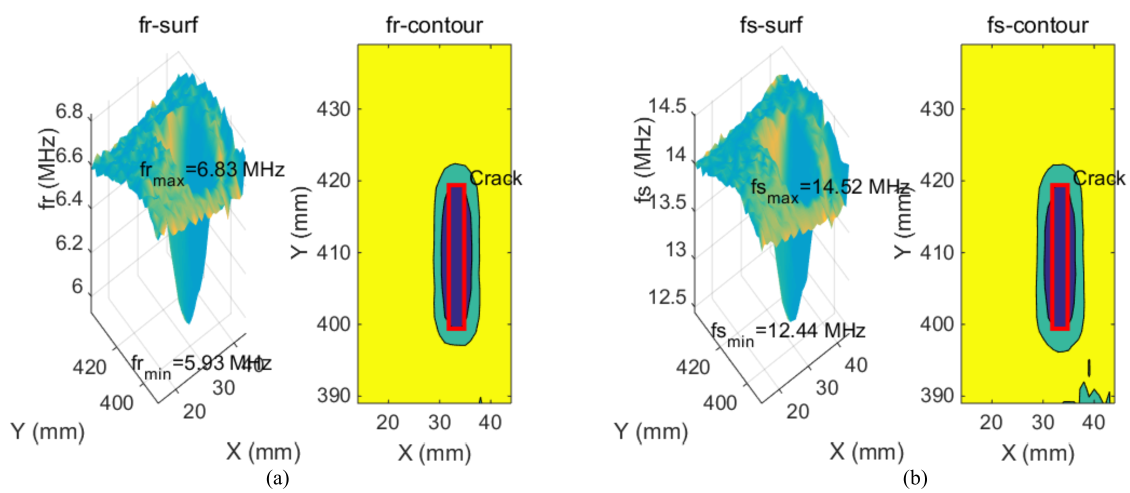


Fig. 12. Steel artificial defect imaged by parameters fusion. (a) Resonance frequency. (b) Series resonant frequency.

## VI. Conclusion

In this article, an innovative method to obtain ECT sensor topology circuit each parameter was proposed by deriving an equivalent conversion between ECT sensor topology circuit and piezoelectric crystal topology circuit. This method was first validated by a COMSOL-based virtual instrument, which was designed in the lab. Then, the verification measurements of various coils were demonstrated. Finally, the following conclusions can be drawn.

1) The bridge between piezoelectric field and ECT sensor is constructed though the proposed equivalent conversion in (7). The parameter measurement technology in piezoelectric field is introduced into ECT sensor. Therefore, a method of measuring coil topology circuit each parameter (rather than partial parameters) is proposed.
2) A virtual VNA based on COMSOL is designed to obtain coil's frequency response. Thus, the accuracy of inductance and capacitance measurement of the proposed method can be verified by the proposed virtual instrument and simulation.
3) The obtained experimental results validate the effectiveness of the proposed method. It can be indicated in three part: take the measurement result of impedance analyzer as the standard value, the inductance measurement error is as less as 3%, and inductance measurement can separate the influence caused by coaxial cable length variation. The STD of inductance measured in different coaxial cable lengths is as low as 0.02. So, the capacitance change caused by coaxial cable length can be identified. The measured capacitance is linear to the length of the coaxial cable, which indirectly verifies the accuracy of capacitance measurement. Metal cracks can be effectively imaged by not only inductance and resistance but also winding capacitance. Moreover, more parameters provide potential value for multiparameter fusion to improve SNR or sensitivity.

Through the proposed ECT sensor multiparameters measurement and separation method, the physical effects of ECT sensor can be separated and the observation dimension is increased. Not only the inductance but also the winding capacitance and resistance can be separated by the proposed method. Compared to traditional ECT sensors, this method provides additional parameters as winding capacitance in characterizing metal surface morphology or coaxial cable length and resistance in characterizing conductivity variations due to crack or stress. Furthermore, this method provides a potentiality to increase the SNR or sensitivity by multiparameters fusion and reorganizing the weights of various physical effects on the ECT sensor.

The main limitation of this method is that the average solution time of nonlinear partial differential equations can reach as high as 40 s, and it is not suitable for real-time application.

Future work will focus on higher frequency application (exceeds 100 MHz) and multiphysical information identification. The higher observation dimension provided by multiparameters will be used to separate stress, lift-off, or surface morphology.

## REFERENCES


[1] K.-M. Lee, B. Hao, M. Li, and K. Bai, "Multiparameter eddy-current sensor design for conductivity estimation and simultaneous distance and thickness measurements," *IEEE Trans. Ind. Informat.*, vol. 15, no. 3, pp. 1647–1657, Mar. 2019.

[2] U. Zanovello, M. Borsero, D. Giordano, L. Zilberti, F. Maggiorelli, and G. Tiberi, "Experimental setup to compare measurements and numerical simulations in magnetic resonance imaging RF dosimetry," *IEEE Trans. Instrum. Meas.*, vol. 66, no. 6, pp. 1208–1216, Jun. 2017.

[3] B. L. Cannon, J. F. Hoburg, D. D. Stancil, and S. C. Goldstein, "Magnetic resonant coupling as a potential means for wireless power transfer to multiple small receivers," *IEEE Trans. Power Electron.*, vol. 24, no. 7, pp. 1819–1825, Jul. 2009.

[4] J. R. S. Avila, M. Lu, R. Huang, Z. Chen, S. Zhu, and W. Yin, "Accurate measurements of plate thickness with variable lift-off using a combined inductive and capacitive sensor," *NDT & E Int.*, vol. 110, Mar. 2020, Art. no. 102202.

[5] Y. T. Yu, T. Yang, and P. A. Du, "A new eddy current displacement measuring instrument independent of sample electromagnetic properties," *NDT & E Int.*, vol. 48, pp. 16–22, Jun. 2012.

[6] H. Shi *et al.*, "An ultrasensitive debris microsensor for oil health monitoring based on resistance–inductance parameter," *IEEE Trans. Instrum. Meas.*, vol. 70, pp. 1–9, 2021.

[7] G. De Angelis, A. De Angelis, A. Moschitta, P. Carbone, and R. Pintelon, "Online identification of the LC product in coupled resonant circuits," *IEEE Trans. Instrum. Meas.*, vol. 69, no. 7, pp. 4592–4603, Jul. 2020.

[8] X. Yin *et al.*, "A combined inductive and capacitive non-destructive evaluation technique using a single spiral coil sensor," *IEEE Sensors J.*, vol. 21, no. 16, pp. 18187–18196, Aug. 2021.

[9] R. Hughes, Y. Fan, and S. Dixon, "Near electrical resonance signal enhancement (NERSE) in eddy-current crack detection," *NDT & E Int.*, vol. 66, pp. 82–89, Sep. 2014.

[10] T. Funck, A. Müller, and H. Bothe, "Synthetic inductance standards made up of capacitances and gyrators," *IEEE Trans. Instrum. Meas.*, vol. 70, pp. 1–4, 2021.

[11] B. Waltrip and F. Seifert, "A programmable capacitor for inductance measurements," *IEEE Trans. Instrum. Meas.*, vol. 66, no. 6, pp. 1572–1578, Jun. 2017.

[12] K. Shi and D. D. L. Chung, "Unprecedented capacitance-based nondestructive evaluation of steels," *J. Mater. Eng. Perform.*, vol. 28, no. 5, pp. 2573–2587, May 2019.

[13] S. Cho, "Inductance measurements in thin films," *Supercond. Sci. Technol.*, vol. 10, pp. 594–597, Aug. 1997.

[14] N. T. M. Tran, V. D'Elia, L. Callegaro, and M. Ortolano, "A capacitance build-up method to determine LCR meter errors and capacitance transfer," *IEEE Trans. Instrum. Meas.*, vol. 69, no. 8, pp. 5727–5735, Aug. 2020.

[15] D. D. L. Chung and K. Shi, "Sensing the stress in steel by capacitance measurement," *Sens. Actuators A, Phys.*, vol. 274, pp. 244–251, May 2018.

[16] R. N. Setiadi and M. Schilling, "Inductance analyzer based on auto-balanced circuit for precision measurement of fluxgate impedance," *Meas. Sci. Technol.*, vol. 29, May 2018, Art. no. 055007.

[17] R. M. G. Salvador, J. A. G. Parra, and N. N. Castellano, "Characterization and modeling of high-value inductors in ELF band using a vector network analyzer," *IEEE Trans. Instrum. Meas.*, vol. 62, no. 2, pp. 415–423, Feb. 2013.

[18] G. Masilamany, P. Joubert, S. Serfaty, B. Roucaries, and Y. L. Diraison, "Radiofrequency inductive probe for non-contact dielectric characterisations of organic medium," *Electron. Lett.*, vol. 50, no. 7, pp. 496–497, 2014.

[19] C. V. Dodd and W. E. Deeds, "Analytical solutions to eddy-current probe-coil problems," *J. Appl. Phys.*, vol. 39, no. 6, pp. 2829–2838, May 1968.

[20] A. Abderahim, A. T. Mahamat, J. P. Chatelon, D. Pietroy, S. Capraro, and J. J. Rousseau, "Approach of copper losses determination in planar windings," *Electron. Lett.*, vol. 52, pp. 1050–1051, Jun. 2016.

[21] G. Y. Tian, N. Chang, J. Liao, and Z. Zhao, "The research of a frequency-modulated displacement sensor," *Sens. Actuators A, Phys.*, vol. 55, nos. 2–3, pp. 153–156, 1996.

[22] T. P. Theodoulidis and E. E. Kriezis, "Impedance evaluation of rectangular coils for eddy current testing of planar media," *NDT & E Int.*, vol. 35, no. 6, pp. 407–414, 2002.

[23] G. Y. Tian, Z. X. Zhao, and R. W. Baines, "The research of inhomogeneity in eddy current sensors," *Sens. Actuators A, Phys.*, vol. 69, pp. 148–151, Aug. 1998.

[24] X. Huang, D. Liu, Y. Wang, and Y. Chen, "Precise derivation for the equivalent circuit parameters of a crystal resonator with series capacitor," *IEEE Trans. Ultrason., Ferroelectr., Freq. Control*, vol. 59, no. 6, pp. 1316–1317, Jun. 2012.

[25] D. Liu, "A method for measuring equivalent parameters of piezoelectric crystal, inductor or capacitor," China Patent 2020 112 922 439, Nov. 18, 2020.

[26] D. Liu, X. Huang, J. Hu, Y. Tang, and Y. Wang, "Measurement of quartz crystal unit parameters based on the precise derivation of zero phase frequency," *Electron. Lett.*, vol. 53, no. 3, pp. 142–144, 2017.
[27] D. Liu *et al.*, "Method for QCM resonator device equivalent circuit parameter extraction and electrode quality assessment," *Micromachines*, vol. 12, p. 1086, Sep. 2021.
[28] Z. Liu, B. Gao, and G. Y. Tian, "Natural crack diagnosis system based on novel L-shaped electromagnetic sensing thermography," *IEEE Trans. Ind. Electron.*, vol. 67, no. 11, pp. 9703–9714, Nov. 2020.
[29] A. J. Fleming, "A review of nanometer resolution position sensors: Operation and performance," *Sens. Actuators A, Phys.*, vol. 190, pp. 106–126, Feb. 2013.
[30] J. R. Vig. *Quartz Crystal Resonators and Oscillators for Frequency Control and Timing Applications—A Tutorial*. Accessed: Jan. 2000. [Online]. Available: https://www.am1.us/wp-content/uploads/Documents/U11625_VIG-TUTORIAL.pdf

**Dong Liu** received the B.Sc. degree in physics from Sichuan University, Chengdu, China, in 2004, and the M.Sc. and Ph.D. degrees in control science and engineering from the University of Electronic Science and Technology of China, Chengdu, China, in 2010 and 2017, respectively.

He is currently a Research Associate with the School of Automation Engineering, University of Electronic Science and Technology of China. His research interests include crystal oscillators, piezoelectric sensor, humidity sensors, and eddy current sensor.

**Hong Zhang** received the B.Sc. degree from joint program between Nanjing Normal University, Nanjing, China, and Northumbria University, Newcastle upon Tyne, U.K., in 2009, and the M.Sc. and Ph.D. degrees from the School of Electrical and Electronic Engineering, Newcastle University, Newcastle upon Tyne, in 2010 and 2014, respectively.

He is currently an Associate Professor with the School of Electronic and Mechanical Engineering, Fujian Polytechnic Normal University, Fuzhou, China. His major research interests include electromagnetic nondestructive testing, RFID, microwave, communication science, and technology.

Dr. Zhang is a reviewer of many international journals.

**Xiaoting Xiao** received the B.Eng. degree in electronic information engineering from the Chongqing University of Posts and Telecommunications, Chongqing, China, in 2010, the M.Eng. degree from Polytech' Nantes, Nantes, France, in 2012, and the Ph.D. degree in electronic, microelectronic, nanoelectronic, and microwaves from Nantes University & Ifsttar, Bouguenais, France, in 2016.

She has worked as a Post-Doctoral Fellow with the University of Electronic Science and Technology of China, Chengdu, China, from 2016 to 2020. She is currently a Lecturer with Southwest Petroleum University, Chengdu. She has been working in the field of electromagnetic nondestructive testing, especially ground penetrating radar. Her interests include the electromagnetic modeling, imaging algorithms, and the inversion methods for high-resolution nondestructive characterization of civil engineering materials.

**Qiuping Ma** received the B.Sc. degree in electronic information engineering from Sichuan Normal University, Chengdu, China, in 2017. She is currently pursuing the Ph.D. degree in nondestructive testing using eddy current technique with the University of Electronic Science and Technology of China, Chengdu.

Her research interests focus on eddy current testing including near-remote filed eddy current testing and eddy current array.

**Haoran Li** received the B.Sc. degree in electrical engineering and automation and the M.Sc. degree in control science and engineering from the Southwest University of Science and Technology, Mianyang, China, in 2015 and 2018, respectively. He is currently pursuing the Ph.D. degree with the University of Electronic Science and Technology of China, Chengdu, China.

His research mainly focuses on eddy current testing and thermography as well as instrumentation manufacturing.

**Guiyun Tian** (Senior Member, IEEE) received the B.Sc. degree in metrology and instrumentation and the M.Sc. degree in precision engineering from the University of Sichuan, Chengdu, China, in 1985 and 1988, respectively, and the Ph.D. degree from the University of Derby, Derby, U.K., in 1998.

From 2000 to 2006, he was a Lecturer, a Senior Lecturer, a Reader, a Professor, and the Head of the Group of Systems Engineering, University of Huddersfield, U.K. Since 2007, he has been with Newcastle University, Newcastle upon Tyne, U.K., where he has been the Chair Professor in sensor technologies. He is currently an Adjunct Professor with the School of Automation Engineering, University of Electronic Science and Technology of China, Chengdu. He has coordinated several research projects from the Engineering and Physical Sciences Research Council (EPSRC), Royal Academy of Engineering, and FP7; on top of this, he also has good collaboration with leading industrial companies, such as Airbus, Rolls Royce, BP, nPower, Networkrail, and TWI among others in Europe.

**Bin Gao** (Senior Member, IEEE) received the B.Sc. degree in communications and signal processing from Southwest Jiao Tong University, Chengdu, China, in 2005, and the M.Sc. degree (Hons.) in communications and signal processing and Ph.D. degree from Newcastle University, Newcastle upon Tyne, U.K., in 2011.

He has worked as a Research Associate with Newcastle University on wearable acoustic sensor technology, from 2011 to 2013. He is currently a Professor with the School of Automation Engineering, University of Electronic Science and Technology of China (UESTC), Chengdu. His research interests include electromagnetic and thermography sensing, machine learning, and nondestructive testing and evaluation, where he actively publishes in these areas. He has coordinated several research projects from the National Natural Science Foundation of China.

Mr. Gao is a very active reviewer of many international journals and long-standing conferences.

**Jianbo Wu** received the B.Sc., M.Sc., and Ph.D. degrees from the School of Mechanical Science and Engineering, Huazhong University of Science and Technology, Wuhan, China, in 2009, 2010, and 2014, respectively.

He is currently an Associate Professor with Sichuan University, Chengdu, China. His research interests include electromagnetic nondestructive evaluation, electromagnetic sensors, sensor array, and sensor networks.